Received: 27 September 2019 | Revised: 14 February 2020 | Accepted: 27 March 2020
DOI: 10.1002/pip.3276

RESEARCH ARTICLE

WILEY PROGRESS IN PHOTOVOLTAICS

Simulation of performance differences between offshore and land-based photovoltaic systems

S. Zahra Golroodbari | Wilfried van Sark

Copernicus Institute, Utrecht University, Utrecht, 3584 CB, The Netherlands

Correspondence
S. Zahra Golroodbari, Copernicus Institute, Utrecht University, Princetonlaan 8A, 3584 CB Utrecht, The Netherlands.
Email: s.z.mirbagherigolroodbari@uu.nl

Abstract

The purpose of this study is to model, simulate, and compare the performance of a photovoltaics system on land and at sea. To be able to have a fair comparison the effect of sea waves, wind speed and relative humidity are considered in this model. The sea waves are modeled in the frequency domain, using a wave spectrum. The irradiation on a tilted surface for a floating system is calculated considering the tilt angle that is affected by the sea waves. Moreover, the temperature is estimated based on heat transfer theory and the natural cooling system for both floating and land-based photovoltaic systems. Actual measured weather data from two different locations, one located at Utrecht University campus and the other one on the North Sea, are used to simulate the systems, thus making the comparison possible. Energy yield is calculated for these weather conditions. The results show that the relative annual average output energy is about 12.96% higher at sea compared with land. However, in some months, this relative output energy increases up to 18% higher energy yield at sea.

1 | INTRODUCTION

Photovoltaic (PV) solar energy generation capacity has been increasing significantly in the past decade. Its contribution to global electricity supply in 2018 was with 600 TWh almost 2.4%, which is predicted to increase to 22% in 2025, with potential up to 70% (40,000 TWh) in 2050.[1,2] However, development of large utility-scale PV system installations is limited due to (i) the cost and availability of land, (ii) decrease of efficiency at high operating PV cell temperature, and also (iii) potential environmental impact including biodiversity.[3] Therefore, a strong motivation is emerging for introducing both building-integrated PV (BIPV) and floating PV systems, both onshore and offshore.[4] Offshore PV systems are categorized into installations (i) for ships, (ii) as floating PV (FPV), and (iii) on islands. In this study, we will focus on offshore FPV systems and their challenges.

Installation of FPV systems on water firstly saves land that may be otherwise implemented for agricultural use, and secondly, the natural cooling potential of the water body may enhance PV performance, due to higher level of wind speeds offshore, along with the presence of water. In addition to these advantages, a lower amount of obstacles causing shading loss and a lower amount of dust compared with land-based PV (LBPV) systems are further advantages. Moreover, due to the fact that more than 50% of the entire world population lives within 100 km of an oceanic coast, an FPV system installed on sea can be conveniently located to supply energy to these regions.[5,6] Also the extracted energy from FPV systems could be a great supply for offshore platforms and ships and would cancel out 3% global green house gas emission from them.[6] All this is leading to FPV systems becoming a hot topic of research at the moment.

FPV systems are categorized in four main groups with respect to their supportive structures[7]: (1) thin film: no strong pontoon is required as the supporting structure due to low weight of the thin film modules; (2) submerged: it might be installed with or without pontoon; (3) tilted arrays: needs rigid pontoons; and (4) a new approach using microencapsulated phase change material (MEPCM)-based pontoon modules. In Trapani[8] and Trapani and Redón Santafé,[9] many different FPV systems that are built between 2007 and 2013 are reviewed. The common benefits from these installations were identified as (i)

This is an open access article under the terms of the Creative Commons Attribution License, which permits use, distribution and reproduction in any medium, provided the original work is properly cited.
© 2020 The Authors. Progress in Photovoltaics: Research and Applications published by John Wiley & Sons Ltd

reducing water evaporation from the reservoir/pond on which these systems are located and (ii) decreased algal growth. It should be taken into consideration that none of the reviewed research projects was installed at sea or ocean. The following seven different factors may indicate if an FPV system is designed optimally: *modularity, flexibility, robustness, safety, optimum supportive structure size, simplicity of installation, and minimizing the final costs.*[10]

One of the FPV projects that fulfills all the mentioned factors above is the SERIS (Solar Energy Research Institute of Singapore) project located in Tengeh, Singapore.[11] In a comparison between the FPV system of this project and the typical rooftop-mounted PV (RPV) systems in Singapore, it was concluded that the module temperature of the FPV system is generally 5°C to 10°C lower than the RPV systems. As a consequence, the performance ratio is around 10% above that of the RPV system in Singapore. In a research project in South Korea, a 100-kW FPV system is compared with normalized data from a 1-MW land-based PV system on a close-by location.[12] The FPV system was installed over the Hapcheondam reservoir. It was assumed that the irradiation and temperature are the same on both locations. Their results showed that the average efficiency of the FPV system is 11% higher than the LBPV system in that location. In another research project, two FPV systems denoted as floating, tracking, cooling, concentrating (FTCC) systems are developed, one in Livorno and the other at a location near Pisa, both in Italy.[13] They developed a design to cool the panels using water, which increased the efficiency with 15%. It is concluded in this research that with their system considering the cooling system, reflection and sun tracker, the FPV performs annually almost 30% better compared with a similar LBPV system.

A natural cooling system or water cooling has an important role in FPV system performance. In Rosa-Clot and Tina,[14] performance of two submerged panels is compared with a reference panel in a nearby location, all panels are placed in horizontal position. The results show that the submerged panel at a depth of 4 cm below the water level performed much better compared with the other two. Also their results showed that the panel at a depth of 40 cm had the lowest output power for the same conditions, due to light absorption of the water body above the panel. The existence of water helps first to cool the panel and second to keep the temperature relatively constant.

In this paper, we develop a model of a small FPV system consisting of 12 panels to be located on the North Sea. The modeling results will at a later stage be compared with the outputs from an experimental system installed on the North Sea. The panels are assumed to be placed on one steel pontoon that is fixed with four wire ropes to four buoys in its surroundings. The wire ropes limit the degree of freedom for the pontoon, in this way dealing with impact from sea waves. The following should be taken into consideration for modeling the FPV system: (i) wind speed: the wind that blows over the sea area causes waves and also changes the apparent panel temperature ($T_{a,p}$) affecting the PV performance; (ii) wave effect: each wave coming toward the pontoon has a certain energy that is able to cause movements of the pontoon and thus can change the orientation and the tilt angle of the panels located at the pontoon in a dynamical way; and (iii) relative humidity: like wind speed, this factor affects $T_{a,p}$. The wave should be mathematically modeled based on these aspects, from which orientation and tilt angle can be calculated.

In this contribution, we will present a method using a flowchart. For its development, we need to study the wave characteristics that are used to derive a mathematical model for the dynamical tilt angle of the pontoon on which the panels are mounted. Both aforementioned issues are functions of wind data at sea. Then, we will compute the irradiation on the tilted surface. To be able to calculate panel performance, both temperature and irradiation data are needed. Therefore, an equilibrium temperature is introduced that is computed from the estimated PV temperature and the fluid (water) temperature. Regarding the natural cooling system, the effect of wind and humidity is considered in the value of $T_{a,p}$ for the system. Finally, the energy yield is calculated. In Section 2, all mathematical models and functions that are required will be described. In Section 3, the abovementioned flowchart is introduced and explained. In Section 4, detailed results will be discussed. The paper will be concluded in the last section.

2 | METHODOLOGY

Modeling an FPV system needs to consider all effective abovementioned aspects that are described in the Introduction section. For calculating the energy yield, we need to compute the performance conditions, that is, surface irradiation and cell temperature. In this study, we assume the FPV to be installed on a pontoon; therefore, both the tilt angle and the orientation may vary, albeit slightly. In this section, we will explain the method. First, we will discuss the irradiation on the tilted surface. Instead of angular reflection losses, we are going to model the system more precisely and calculate the tilt angle in each time interval; because the angular reflection is a function of both latitude and tilt angle.[15] Then, we need to model the wave based on the wind characteristics blowing over the specific region at the North Sea. This is followed by a discussion on the heat transfer and the apparent temperature method. In this discussion, the effects of both wind and humidity on temperature change will be considered.

2.1 | Irradiation over tilted surface

Usually, there is one installed pyranometer for a group of panels, and global horizontal irradiation (GHI) is recorded. But the irradiation on the tilted surface (GTI) determines the power generated by the PV panel. In this section, we will describe how to calculate GTI using the tilt angle, GHI, and some other recorded data.

Global irradiation over the tilted surface (GTI) is calculated from Equation (1):

$$\mathrm{GTI} = \mathrm{DIR}_{\phi} + \mathrm{DIF}_{\phi} + R_{\phi}, \tag{1}$$

where DIR_{ϕ}, DIF_{ϕ}, and R_{ϕ} are direct, diffuse, and reflective irradiance components, respectively, and $\phi = \{\beta, \gamma\}$, where β is surface tilt angle and γ is azimuth angle.

Direct tilted irradiance (DIR_{ϕ}) is calculated as follows:

$$\mathrm{DIR}_{\phi} = B_h \times r_b, \tag{2}$$

where B_h is direct normal irradiance (DNI) and r_b is the direct irradiance conversion factor and calculated via

$$r_b = \max\left(0, \frac{cos\theta}{cos\theta_z}\right) \tag{3}$$

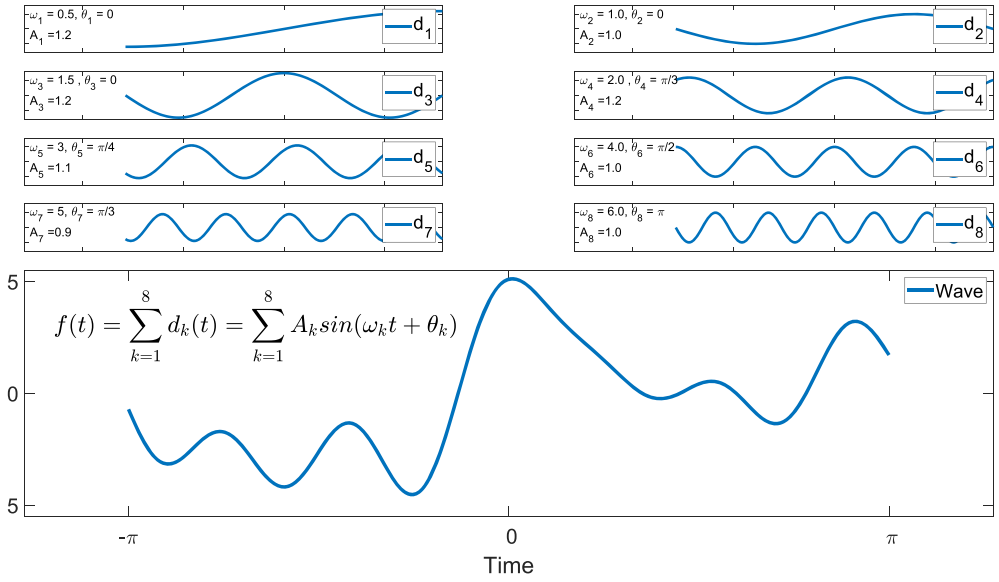


FIGURE 1 Wave decomposition. The wave in the bottom box is composed of the waves shown in the eight top boxes [Colour figure can be viewed at wileyonlinelibrary.com]

with

$$cos\theta = cos\theta_z cos\beta + sin\theta_z sin\beta cos(\gamma_s - \gamma), \tag{4}$$

where θ_z and γ_s are solar zenith and azimuth angles.

Many models have been developed to calculate diffuse tilted irradiance (DIF_ϕ). Their main difference is coming from the fact that these consider the diffuse irradiance being isotropically distributed over the sky dome or not. In this study, we assume the anisotropic model called Klucher model (Kl). DIF_ϕ in this model is estimated via the following equation:

$$DIF_\phi = D_h \times R_{dif}, \quad R_{dif} \geq 0, \tag{5}$$

where D_h is diffuse horizontal irradiance (DHI) and R_{dif} is calculated via the following formula:

$$R_{dif} = R_{d,LJ}\left(1 + f_K cos^2\theta sin^3\theta_z\right)\left(1 + f_K sin^3\frac{\beta}{2}\right), \tag{6}$$

where $R_{d,LJ}$ and f_K are the Liu–Jordan isotropic model diffuse irradiance transposition factors defined in Equation (7) and the Kluchers' conversion factor defined in Equation (8), respectively.[16]

$$R_{d,LJ} = 0.5 \times (1 + cos\beta) \tag{7}$$

$$f_K = 1 - \left(\frac{D_h}{G_h}\right)^2 \tag{8}$$

The classical approach to the modeling of the reflected irradiance (R_ϕ) assumes that reflected rays are diffuse and coefficients of reflection of the direct and diffuse rays are identical.[17] Therefore, R_ϕ is calculated from Equation (9):

$$R_\phi = \rho G_h R_h, \tag{9}$$

where ρ is the foreground albedo = 0.06 calculated for the open ocean surface in American National Snow and Ice Data[18] and $R_h = 0.5(1 - cos\beta)$ is the transposition factor for ground reflection.

2.2 | Wave model

Each wave can be seen as a combination of many small waves with different characteristics. Thanks to Joseph Fourier (1768–1830) for developing Fourier decomposition, all complex wave forms can be reproduced with an infinite sum, or series, of simpler functions. Mathematically, the complex wave $W(t)$ in the time domain can be described as in Equation (10):

$$W(t) = \sum_{k=1}^{\infty} A_k \cos\left(\omega_k t + \theta_k\right), \tag{10}$$

where A_k is amplitude (or Fourier coefficient), ω is angular frequency, and θ is phase angle.

Figure 1 shows a very simple example for wave decomposition; the wave in the bottom box, denoted by $f(t)$ in the figure, is the final wave that results from the summation of all single frequency waves (d_1 to d_8) with characteristics shown in the above subplots, where it can be seen that the wave frequencies are increasing from the first to the eight component. Note that A_k values differ slightly from each other. It is quite complicated to study the wave in the time domain, which is why in this study we discuss wave characteristics in the frequency domain. This so-called wave spectrum will be discussed in this subsection.

Wind is mainly responsible for wave generation at sea. A wave can be described using frequency (f), wavelength (λ), time period (T), amplitude (a), and height (H), which is double the amplitude. In this model we considered the wave energy and its conversion to force. The amount of force from a wave may move the pontoon and is responsible for the tilted angle of the panel surface.

The energy density and power density of a harmonic wave can be calculated from the following equations[19]:

$$E_{Density} = \frac{\rho_{water} g H^2}{8}, \quad P_{Density} = \frac{E_{Density}}{T}, \tag{11}$$

where g is gravitational constant 9.81 m/s^2.

Following linear wave theory, wave energy per unit crest width for a specific wave is calculated as shown in Equation (12):

$$E = \frac{\rho g H^2 \lambda}{8} \quad (\text{J/m}). \tag{12}$$

Maximum power under ideal conditions is proportional with the calculated energy and per meter of the wave front and is equal to

$$P_{ideal} = \frac{1}{32\pi}\rho g^2 H^2 T \quad (\text{W/m}). \tag{13}$$

However, obtaining these parameters for irregular waves or real waves should be calculated in a different way. To this end, the wave characteristics at fully developed open seas are generated by the

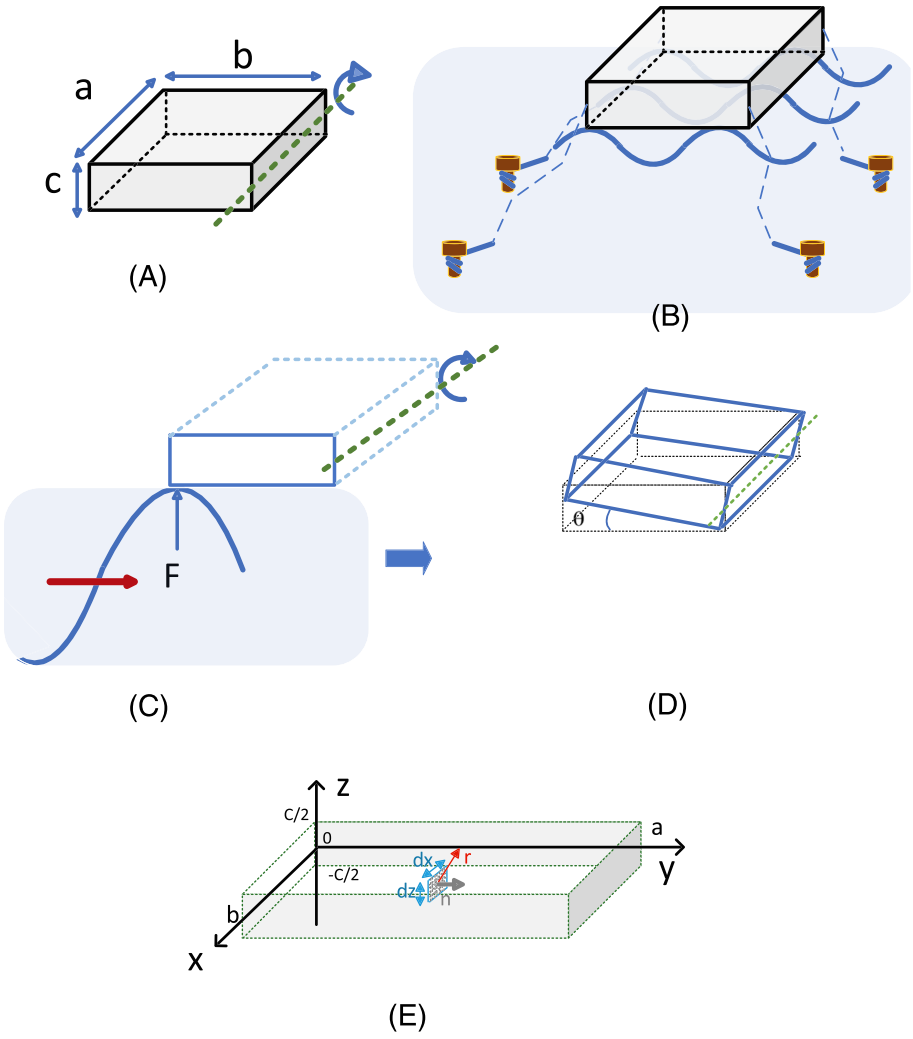


FIGURE 2 (A) Pontoon's dimension, (B) pontoon at sea level, (C) torque τ touches the pontoon and tries to rotate it around the shown axis, (D) pontoon rotated by θ, (E) coordinates and the pontoon dimensions [Colour figure can be viewed at wileyonlinelibrary.com]

so-called Joint North Sea Wave Project (JONSWAP) spectrum (JS) as shown in Equation (14).[20,21] This spectrum is a fetch-limited wind wave spectrum, which was developed for the North Sea by the offshore industry and is used extensively. The elevation $S(\omega)$ of (linear) fully developed open seas is described as

$$S(\omega) = \alpha \frac{g^2}{\omega^2} \exp\left[-\frac{5}{4}\frac{\omega_p}{\omega}^4\right] \gamma^r, \tag{14}$$

$$r = \exp\left[-\frac{1}{2}\frac{\omega - \omega_p}{\sigma\omega_p}\right], \tag{15}$$

$$\alpha = 5.061\left(\frac{\omega_p}{2\pi}\right)^4 H_s\left[1 - 0.287\log\gamma\right], \tag{16}$$

where ω_p is peak spectrum angular frequency, γ is a peak enhancement factor, and H_s is significant wave frequency and $\sigma = 0.07$ for $\omega < \omega_p$ and $\sigma = 0.09$ for $\omega \geq \omega_p$.

For a real wave, which does not consist of only one sinusoidal wave with one frequency, the wave energy and maximum power, per unit meter, will be calculated as shown in Equations (17) and (18), respectively.

$$E = \rho g \int_0^\infty S(\omega) d\omega, \tag{17}$$

$$P = \rho g \int_0^\infty v_g S(\omega) d\omega, \tag{18}$$

where v_g is group velocity and for deep water conditions $v_g = g/2\omega$.[22]

With calculating this values and knowing the pontoon's weight and dimensions, we are able to estimate the tilted angle for the pontoon as a function of time. Let us assume that the energy from wave is transferred to rotating kinetic energy that can rotate the pontoon, for example, about an axis in line with its length.

$$E_R = \frac{1}{2} I \omega_r^2, \tag{19}$$

where E_R is the rotating kinetic energy, I is moment of inertia, and ω_r is angular velocity for the pontoon. Figure 2a,b depicts the pontoon with length, width, and height of *a*, *b*, and *c*, respectively. In the following, first, we discuss how to calculate the moment of inertia and then explain how to use it for calculating the tilt angle. The fundamental definition for moment of inertia is presented in 4 (20):

$$I = \int_0^m r^2 dm, \tag{20}$$

where *m* is mass of substance and *r* is the radius from the axis. It is assumed that the pontoon is symmetrical regarding the *z* axis shown in Figure 2e. Now, let us assume that the coordinates are chosen such that the point $z = 0$ is at the middle of the pontoon's height. A small rectangle inside the pontoon is considered, while its normal vector is parallel with the *y* axis (rotational axis) and its radius from that axis is *r*. Regarding these assumptions, the following proportional equation is valid:

$$\frac{dm}{dxdz} = \frac{m}{bc}. \tag{21}$$

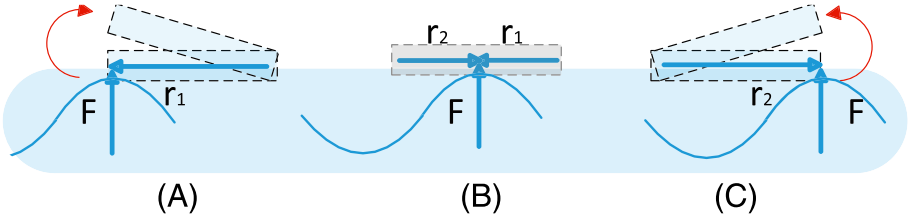


FIGURE 3 Force and radius vector in different positions when wave crest touches for the first time. (A) The left side, (B) middle, and (C) right side of the pontoon [Colour figure can be viewed at wileyonlinelibrary.com]

Therefore, Equation (20) can be changed to

$$I = 2 \times I_{1/2} = 2 \times \int_0^b \int_0^{\frac{c}{2}} \frac{m}{cb} \left(x^2 + z^2\right) dzdx. \tag{22}$$

By solving this, the moment of inertia for the described pontoon and the rotating axis is calculated as follows:

$$I = \frac{1}{3}mb^2 + \frac{1}{12}mc^2. \tag{23}$$

However, the moment of inertia for the pontoon such that the rotating axis is assumed to be on the x axis is calculated in Equation (24):

$$I' = \frac{1}{3}ma^2 + \frac{1}{12}mc^2. \tag{24}$$

For the assumed rectangular pontoon, we have

$$a = 5b \;\&\; a \gg c \;\&\; b \gg c \Rightarrow I' \simeq 5I. \tag{25}$$

Therefore, comparing to rotation around the y axis, rotation around the x axis is negligible, for $a \gg b$. Thus, in this paper, as shown in Figure 2c, we only consider 2D motion for the pontoon, and once the wave crest touches the pontoon, a perpendicular force makes a torque τ as in Equation (26):

$$\tau = \vec{F} \times \vec{r_1}, \quad |r_1| = b, \tag{26}$$

thus trying to rotate the pontoon clockwise, as shown in Figure 2 d, which shows a change in tilt of θ.

Figure 3 shows that the wave forces move while the wave is moving forward. Therefore, for simplicity, we assume that the wavelength and the width of the pontoon has the following relation:

$$\lambda \geq b. \tag{27}$$

Hence, the variation for θ can be described as follows:

1. When the crest of the wave touches the pontoon, as shown in Figure 3a, torque is calculated as mentioned above in Equation (26), which causes the pontoon to rotate clockwise at an angle θ.
2. The wave moves forward and touches the middle of the pontoon, this situation can be translated using linear algebra to the following equation,

$$\tau = \vec{F} \times (\vec{r_1} + \vec{r_2}), \; |r_1| = |r_2| = b/2 \tag{28}$$

due to the symmetrical characteristics of the pontoon the vectors $\vec{r_1}$ and $\vec{r_2}$ are in opposite direction and have equal magnitude so the total torque is equal to zero, which means that the normal vector for the pontoon at this scenario is $\pi/2$ and the pontoon makes an angle of $\theta = 0$.
3. This scenario is similar to scenario (a), but the $\vec{r_2}$ is in the opposite direction that makes the pontoon to rotate anticlockwise at angle θ. In comparison with scenario (a), the absolute value of the tilt angle is the same, but the orientation of the pontoon is different.

2.3 | Heat transfer and equilibrium temperature

One of the main issues we need to consider in this model is the heat transfer for both systems. In the FPV system, the pontoon is constantly in contact with the sea water, and in LBPV, the platform that is assumed to be made exactly with the same material and in the same size is in contact with air. The heat transfer in two systems is discussed in this section. The equilibrium temperature should be calculated, which is the temperature after heat transfer from the PV side to the fluid side that might be either water or air. Calculating this value needs some consideration for the PV side temperature that is not measured, therefore, we estimate the initial operating temperature of a PV cell using the servant correlation,[23] as follows:

$$T_c = T_a + \alpha\,(1 + \beta T_a)\,(1 - \gamma v)\,GTI, \tag{29}$$

where T_a is ambient temperature, v is wind speed, and α, β, and γ are constants that depend on the specific PV module structure. We need to solve the thermal equilibrium problem between the pontoon/platform and the fluid around these, following Equation (30), to calculate the equilibrium temperature:

$$m_p c_p \Delta T_p = m_f c_f \Delta T_f, \tag{30}$$

where $m_{p,f}$ is mass of substance, $c_{p,f}$ is heat capacity, and $\Delta T_{p,f}$ is temperature difference. Indices p, f denote pontoon/platform and fluid, respectively. The formula can be rewritten as, with T_{Eq} the equilibrium temperature

$$m_p c_p (T_{PV} - T_{Eq}) = m_f c_f (T_{Eq} - T_f). \tag{31}$$

It should be taken into consideration that the PV panels after heat transfer perform at the equilibrium temperature, obviously in equilibrium $T_{Eq} = T_{PV} = T_f$. Note that due to the large heat conductivity of steel, the heat transfer rate is fast.

2.4 | Cooling effect and apparent temperature

The recorded ambient temperature alone is not sufficient for performance analysis, as is evident from the servant correlation[23] that also takes into account the effect of other weather conditions, for example, wind speed (WS) and humidity. For example, in Huld et al.,[24] the PV performance all over the world is studied considering the wind speed effect as well as ambient temperature and local irradiation. However, in this paper, a more generic overview is needed, which is why the effect of humidity is also considered. We therefore use the so-called apparent temperature. In Jacobs et al.,[25] the following equation is implemented to incorporate the effects of air temperature, humidity, and wind speed.

$$T_A = T_{db} + 0.33p_v - 0.7|v| - 4, \tag{32}$$

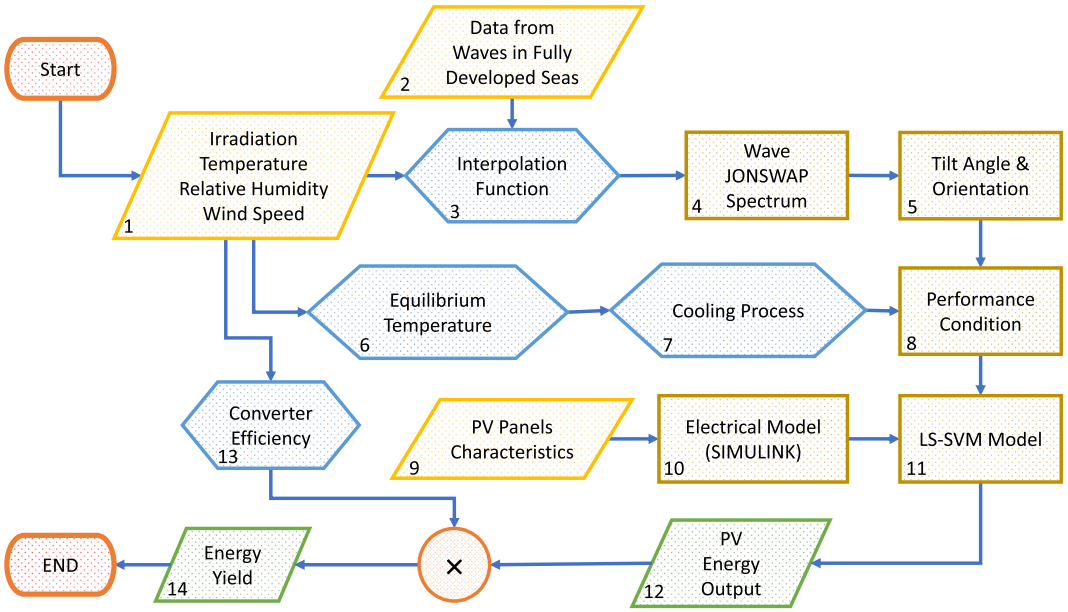


FIGURE 4 Model flowchart. JONSWAP, Joint North Sea Wave Project; LS-SVM, least square support vector machine; PV, photovoltaic [Colour figure can be viewed at wileyonlinelibrary.com]

where T_A is apparent temperature (°C), T_{db} is dry bulb temperature (^oC), v is the wind speed at 10-m height (m/s), p_v is the vapor pressure of air (hPa) and can andbe computed from Equation (33).[26]

$$p_v = \exp\left(1.8096 + \frac{17.69D}{273.3 + D}\right), \tag{33}$$

where D(^oC) is dew point temperature computed from the simple approximation formula,

$$D = T - \frac{100 - RH}{5}, \tag{34}$$

where RH is the relative humidity, where it is assumed that RH is larger than 50%.[27] In this work, the apparent temperature is implemented as the effective temperature rather than to consider not only bulb dry temperature but wind speed and relative humidity as well.

3 | MODEL SET-UP AND SIMULATIONS

Figure 4 depicts a flowchart according to which both systems are modeled. The flowchart has 14 numbered boxes, each of which represents a process, function, or documented data. In this section, each box will be discussed, and the mathematical model related to the box will be addressed regarding Section 2. The implementation of the model is done using a MATLAB environment.

Box 1: Ambient data

Measured ambient data are taken from both the Utrecht Photovoltaic Outdoor Test (UPOT) facility and the Royal Netherlands Meteorological Institute (KNMI) website and are used to make the result statistically tangible.[28,29] As mentioned in the flowchart, data in this part consist of (i) irradiation (global horizontal, W/m^2), (ii) temperature (°C), (iii) relative humidity (a.u), and (iv) wind speed (m/s). The available recorded values for wind speed are maximum and minimum values per day. As we need data for our time resolution of 1 min,

TABLE 1 Waves in fully developed seas[30]

Wind speed (km/hr)	Average period (s)	Wave height (m)
20	3.2	0.5
30	4.6	1.2
40	6.2	2.5
50	7.7	4.5
60	9.9	7.1
70	10.8	10.3
80	12.4	14.3
90	13.9	19.3

an approximation is done. Assuming the fact that the data are normally distributed and by using the empirical rule in Equation (35), we approximated the data with the desired time resolution.

$$Pr\,(\mu - 2\sigma \le X \le \mu + 2\sigma) \approx 0.9545, \tag{35}$$

where X is an observation from a normally distributed random variable, μ is the mean of the distribution, and σ is its standard deviation.

Box 2: Data from waves in fully developed seas

For quantification of the waves using the wave model, we implemented the recorded data in Table 1. These data specify a variety of predicted wave properties for fully developed seas at different wind speeds.[30] With this table and with knowledge about the wind speed, the average period and wave height can be estimated with good accuracy.

Box 3: Interpolation function

Data tabulated in Table 1 are discreet and need to be changed to a continuous function. Therefore, a cubic interpolation method is implemented to generate this continuous function.

Box 4: Wave JONSWAP spectrum

As discussed in Section 2, modeling the wave in the time domain is complicated, so a frequency domain model is chosen. In this box, the

wave JONSWAP spectrum is generated. The JONSWAP spectrum is mathematically shown in Equation (14). Using actual wind speed data using interpolation of data in Table 1, wave spectra are generated. It is assumed that the wave spectrum for every single day is unique. For instance, Figure 5 shows JONSWAP spectra for all days in August 2016, using wind speed data from KNMI.[28] Having a look at this figure can easily give us an intuitive impression about the days in which the sea is calm, and we may have less strong waves, which is in fact the case for most of the days. However, later, we will show how the waves change the tilt angle for the pontoon where the panels are assumed to be mounted on.

Box 5: Tilt angle and orientation

By using the wave spectrum for each day, the tilt angle can be computed using information in Section 2.2, and as a result, the irradiation over the tilted surface (GTI) is calculated, using the model of Section 2.1. Figure 6 shows the calculated tilt angle for the pontoon in the FPV system. The angles are estimated based on the wave spectrum shown in Figure 5. For most of the days, when the sea is calm, tilt angles vary only slightly between 0° and 3°. For some days, the tilt angles exceed 10°, and only for one day, tilt angles reach 20°.

For calculating power in the *i*th time window of the day, we have the data set *i* consisting of panel orientation and tilt, which are considered in 2D such that the pontoon varies only between two orientations that are the southeast and northwest. The data set is shown in Equation (36):

$$[(\beta_i, \gamma_1), (\beta_i, \gamma_2)], \tag{36}$$

TABLE 2 PV panel characteristics

V_{OC} (V)	I_{SC} (A)	V_{MPP} (V)	I_{MPP} (A)	P_{MPP} (W)	Efficiency (%)	Temp coeff power (%/K)
39.9	10.3	32.9	9.4	310	19.35	−0.375

where γ denotes the azimuth angle and $\gamma_1 = 135°$ and $\gamma_2 = 315°$ and β_i is the tilt angle in the *i*-th time period. This means that in this study, for each tilt angle, we considered two azimuth or orientation values, one toward the southeast and other toward the northwest. Simulating of this part is done by implementing the PV_LIB toolbox[31] in MATLAB environment.

Box 6: Equilibrium temperature

It should be taken into consideration that the cell temperature is different from the ambient temperature. Thus, as discussed in Section 2.3, the PV cell temperature is calculated using the servant correlation, Equation 29. The heat transfer process makes heat to transfer across the boundary of the system. Therefore, the PV equilibrium temperature should be calculated using Equation (31). Fluids around the pontoon/platform are infinite; however, in this study, we only consider that the same volume of the fluid is effective in heat transfer in a unit of time. For the FPV system, the sea water changes the PV initial operating temperature effectively as the pontoon is in touch with the water, but in LBPV the fluid is the air.

Box 7: Cooling process

As discussed in Section 2.4, to consider the effect of relative humidity and wind speed, we impose the apparent temperature using Equation (32). Regarding the discussion in that section, the wind speed has a linear, and relative humidity has a nonlinear relation with the apparent temperature.

Box 8: Performance condition

In this box, we consider both GTI and working temperature for the PV panels. Regarding these information, we can calculate the output power that is generated by the panels.

Box 9: PV panels characteristics

The PV panels characteristics at standard test conditions (STC), which are defined as 1,000 W/m^2 irradiance, 25°C cell temperature, and air mass (AM) 1.5 solar spectrum, are shown in Table 2. These data

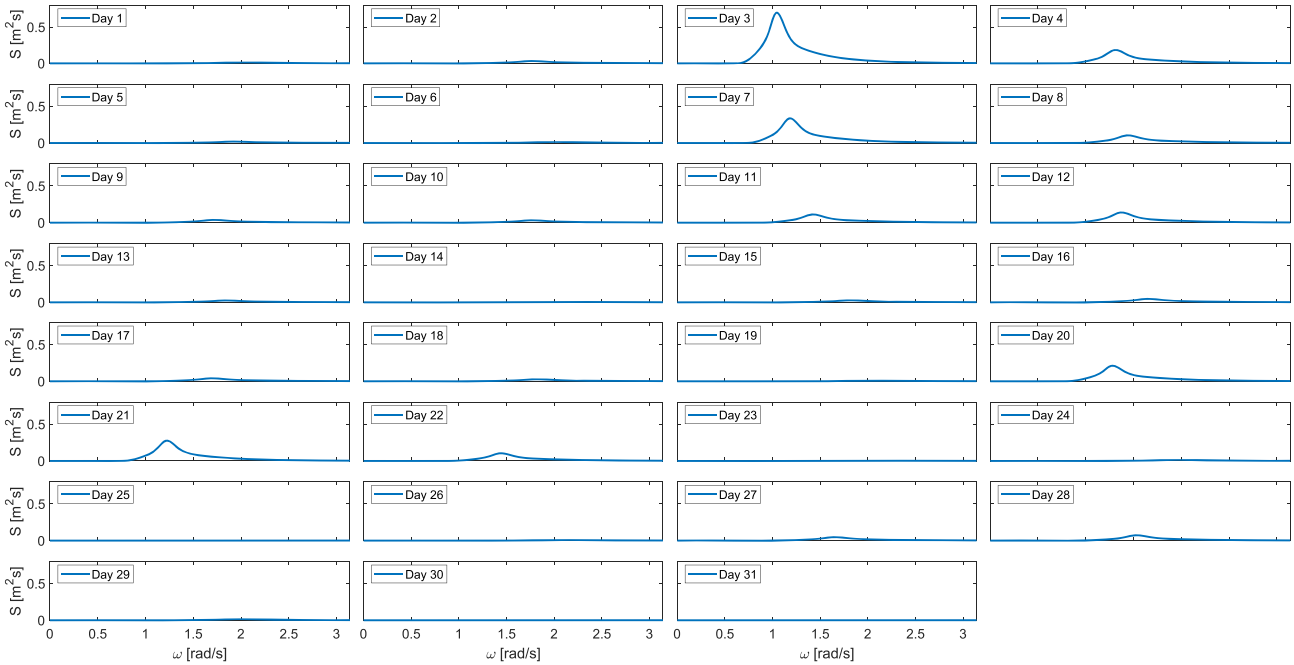


FIGURE 5 Joint North Sea Wave Project (JONSWAP) spectrum (JS) for all days of August 2016 [Colour figure can be viewed at wileyonlinelibrary.com]

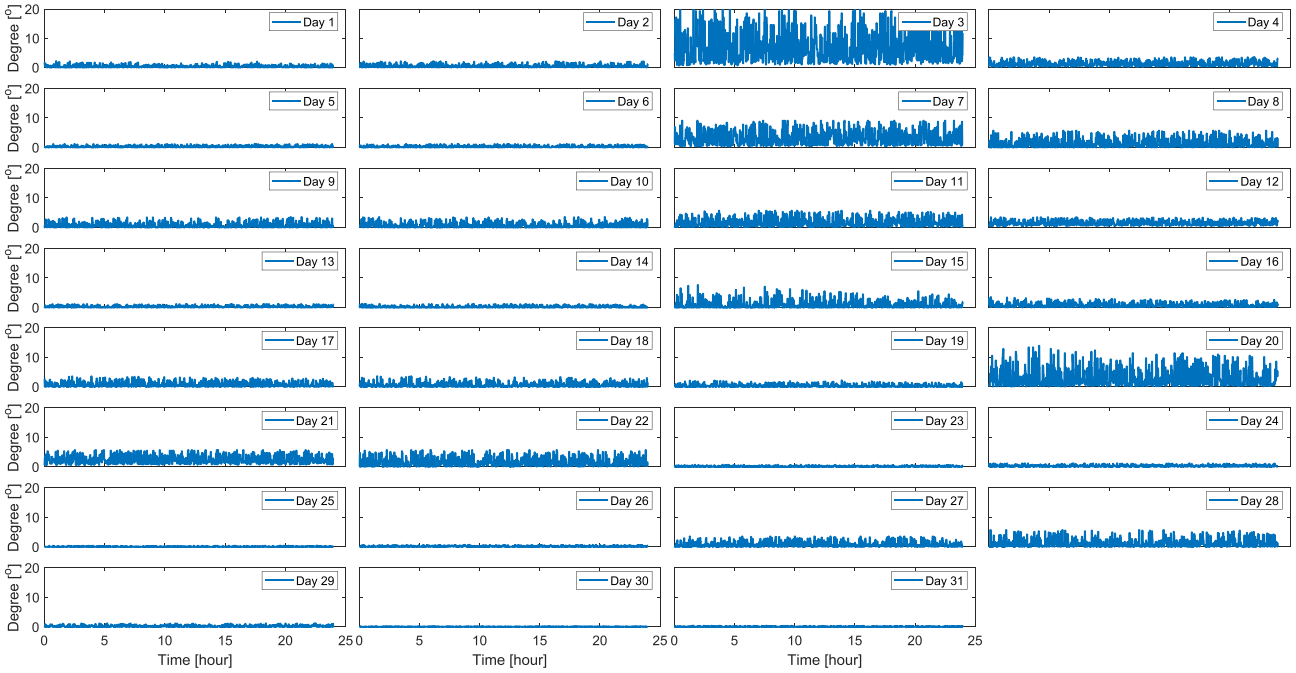


FIGURE 6 The tilt angle of the pontoon for all days of August 2016 [Colour figure can be viewed at wileyonlinelibrary.com]

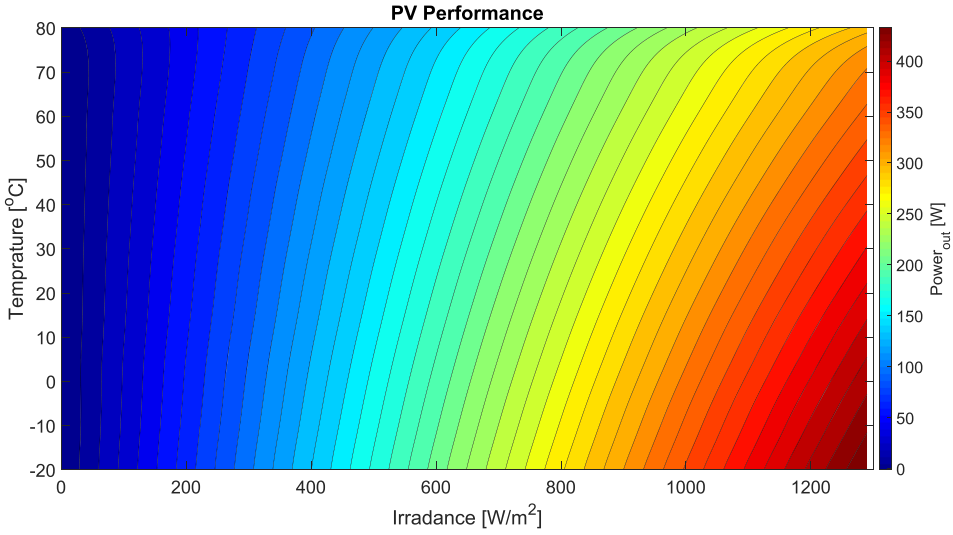


FIGURE 7 Photovoltaic (PV) performance model using least square support vector machine (LS-SVM) [Colour figure can be viewed at wileyonlinelibrary.com]

are extracted from the specification data sheet of the used Exasun X60-BG310 module that is a 310 Watt power module.

Box 10: Electrical model

To simulate the behavior of the full PV system first, one panel is modeled in MATLAB SIMULINK, and a set of data with different irradiation and temperature is computed and recorded via this model. That is based on the PV panel characteristics and is used for data input to a least square support vector machine (LS-SVM) algorithm. In our system, we use 12 identical panels, thus having a system capacity of 3.72 kWp.

Box 11: LS-SVM model

The LS-SVM PV performance model is developed based on the LS-SVM algorithm.[32] The information extracted from the electrical model is used for training of the intelligent algorithm. The training data set of

$$T_{VM} = \{(x_1, y_1), \ldots, (x_l, y_l)\}, \tag{37}$$

where $x(j) = [G(j), T(j)]^{T_{VM}}$, $y(j) = P(j)$, $j = 1, \ldots l$ is recorded from the MATLAB SIMULINK file. In this data set, G is the irradiation level, T is ambient temperature, P is PV output power, and j is the number of elements in the data set. The least square support vector machine uses the training data set (T_{VM}) to estimate the optimal nonlinear regression function $\hat{f}$, Equation (38), mapping the input data that are the performance conditions (from Box 8) to the PV output.[33]

$$\forall\, G, T: \; [G \;\; T] \underset{\rightarrow}{\hat{f}} P \tag{38}$$

Figure 7 depicts performance of aforementioned module in wide range of irradiation and temperature. This PV performance is modeled implementing LS-SVM algorithm.

Box 12: PV energy output

This box contains the computed output power for the panels in both systems. The time resolution of this data is 1 min, and thus, the output energy is calculated.

Box 13: Converter efficiency

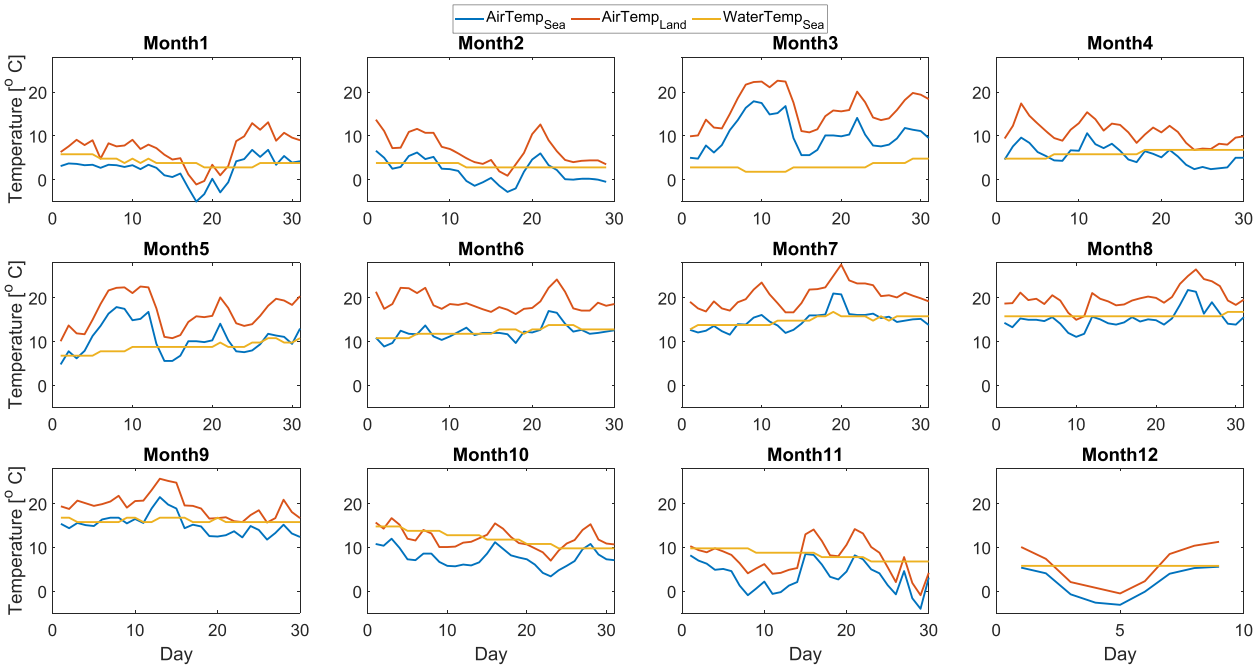


FIGURE 8 Comparison of average daily temperature for both system locations and sea water temperature [Colour figure can be viewed at wileyonlinelibrary.com]

The modular system designed for this test subject is assumed to have one optimizer per panel. The optimizer used is a DC–DC converter, which is controlled with a maximum power point tracking (MPPT) algorithm. The final voltage output in this system is assumed to be 24VDC on a DC bus where all of the loads can be connected. The converter that is assumed to be used in this test set up is SmartSolar MPPT 75/15 designed by Victron Energy.[34] The optimizer controls the output power such that always the output power from each panel is maximum. However, its efficiency depends on temperature as well. The maximum efficiency for this specific optimizer is 98% according to its data sheet. A practical method for predicting the temperature-related power losses for buck converter is implemented in this study.[35] The apparent temperature for both systems is implemented in this model to estimate the converter efficiency at that level of temperature.

Box 14: Energy yield

Shown in Equation (39), the energy yield is computed as a product of output power and converter efficiency.

$$E_Y = \left(\eta_{conv} \times \sum_{n=1}^{N} P_n \Delta t_n\right) \times 10^{-3}, \tag{39}$$

where E_Y is generated energy in kWh, P_n is the power for the time resolution in W, Δt_n is the time resolution in minutes, N the total number of time intervals, n the time interval index, and η_{conv} is the converter efficiency. To calculate daily energy yield, $N = 1{,}440$, as the time resolution is 1 min.

4 | RESULTS AND DISCUSSION

In this section, we will review the results in detail. The results that will be discussed hereafter are extracted from the aforementioned model using the data for the year 2016. First, the effect of wind on both temperature and tilt angle will be shown and discussed. Thereafter, the equilibrium and apparent temperature results for both systems will be compared, and then the tilt angle for the FPV system will be analyzed. Finally, the energy yield for both systems will be compared. The data for LBPV are recorded at Utrecht University campus and data for FPV system from KNMI website.[28,29] It should be noted that the irradiation data for December 2016 are not complete and are only available for 9 days.

At the beginning, let us compare both systems initially: Figure 8 depicts the average daily temperature at the locations where each FPV and LBPV systems are assumed to be installed, for the 12 months of the year. Also the water surface temperature for FPV at North Sea is included. It is clearly shown that although the air temperatures vary over a large range, the sea water surface temperature changes only gradually every month. Minimum air temperature at LBPV is −1.1°C, which is roughly 4°C higher than the minimum temperature at the FPV location. Similarly, the maximum air temperature is higher at the LBPV location. The minimum and maximum sea surface temperature are 1.8°C and 16.7°C, respectively.

Figure 9 shows the apparent temperature at both locations for FPV and LBPV systems. The apparent temperature at sea is much lower than on land due to a higher level of relative humidity in combination with higher wind speeds. As mentioned in Section 2.4, the natural cooling system for FPV is driven by wind speed and relative humidity. From the data recorded in 2016, the average ambient temperature difference for the two locations is 5.05°C, whereas the difference between the apparent temperature for the two locations is nearly twice larger at 9.36°C. The average wind speed difference between two locations is 3.76 m/s, also the relative humidity on average is 8.1% higher in the FPV location.

Figure 10 depicts equilibrium and ambient temperature for both FPV and LBPV systems, also it shows the sea surface temperature. The

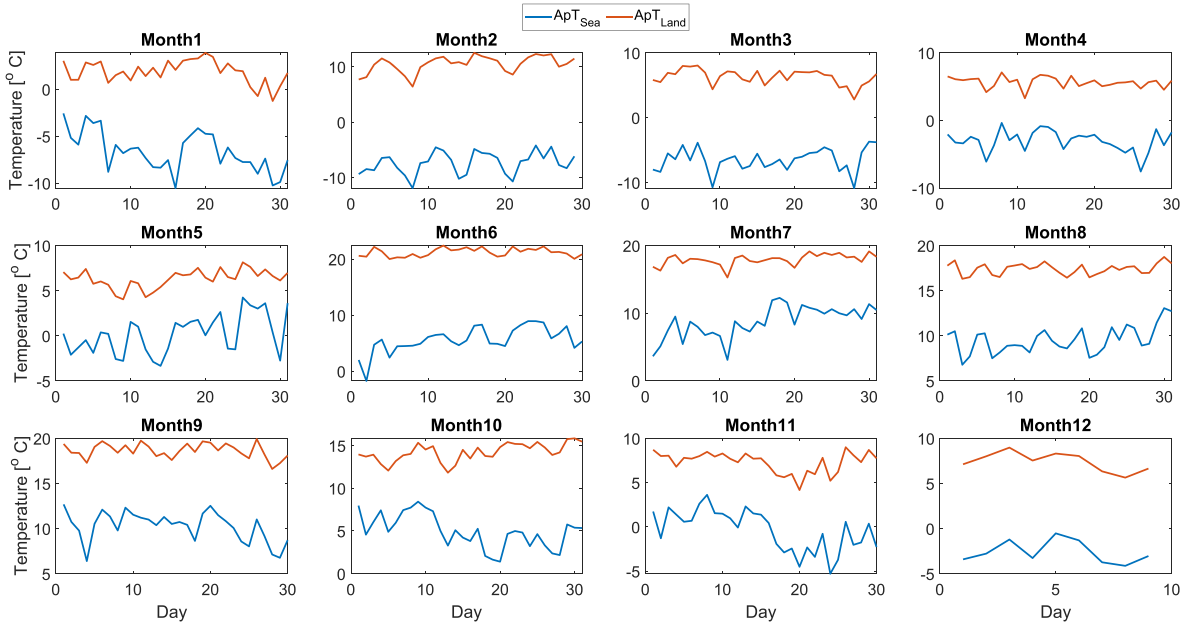


FIGURE 9 Apparent air temperature for both systems [Colour figure can be viewed at wileyonlinelibrary.com]

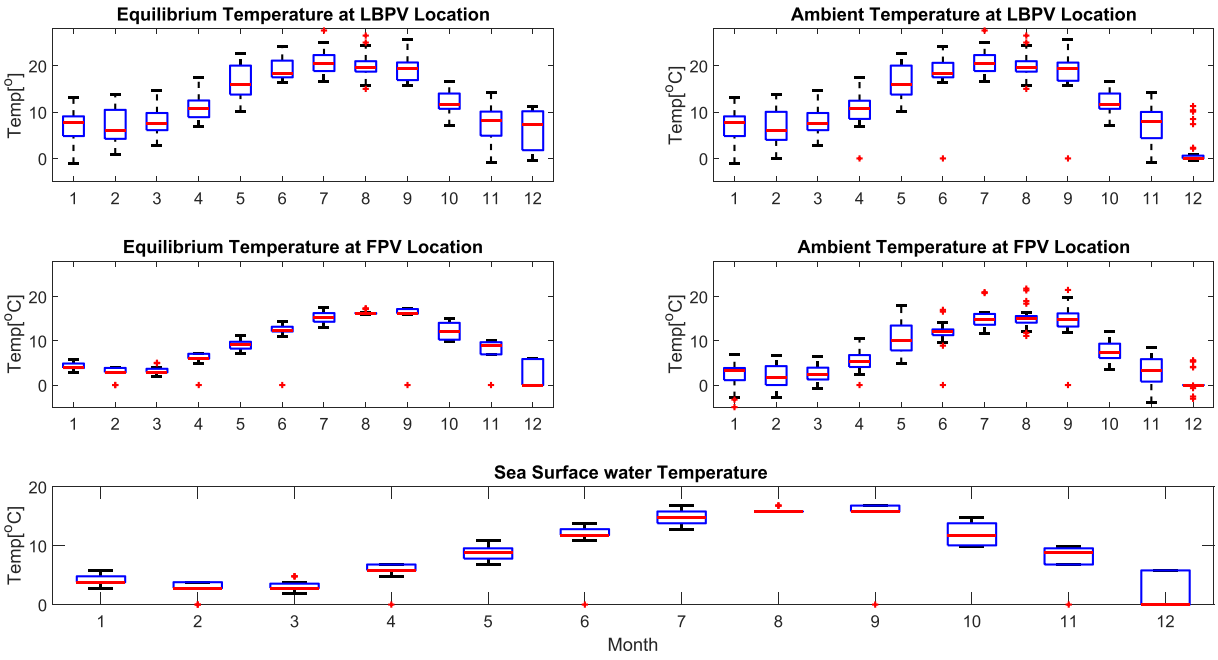


FIGURE 10 Equilibrium and ambient temperature for both systems, and sea surface temperature, for the year 2016 [Colour figure can be viewed at wileyonlinelibrary.com]

TABLE 3 Substances heat characteristics

Substance	Water	Air	Steel
Density (kg/m^3)	1,025	1.225	8,050
Heat capacity (J/K)	4,200	1,005	490

box plots confirm that all temperatures follow a similar trend during the year. However, the difference between the equilibrium and ambient temperature for FPV compared with LBPV system is significant.

As shown in this figure, the sea surface temperature is close to the PV system equilibrium temperature. Regarding the heat transfer theory that is discussed in Section 2.3, Equation (31), this indicates how close the equilibrium is to the fluid temperature. As mentioned before, to limit the fluid with infinity volume, it is assumed that the effective volume of the fluid is as large as the platform/pontoon volume. To this end, the substance density and heat capacity of water, air (at sea level), and steel is compared in Table 3. Considering Equation (31) and the table context, it is clearly shown that the equilibrium temperature in the FPV system is much closer to the sea surface temperature and in the LBPV system it is much closer to the PV temperature itself. However, the effect on the equilibrium temperature of wind and humidity is clear. Note that the variation of the equilibrium temperature for the FPV system is much smaller than the variation for the LBPV system (the boxes are much narrower).

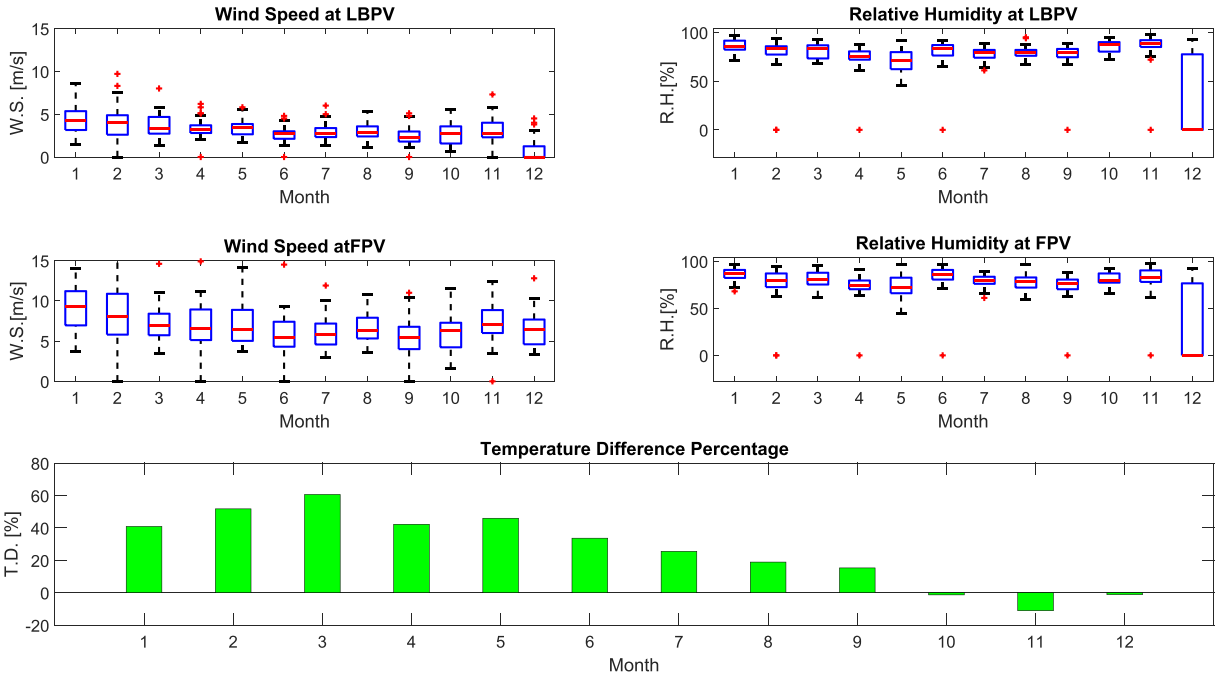


FIGURE 11 Wind speed, relative humidity, and relative difference of equilibrium temperature for both systems, for the year 2016 [Colour figure can be viewed at wileyonlinelibrary.com]

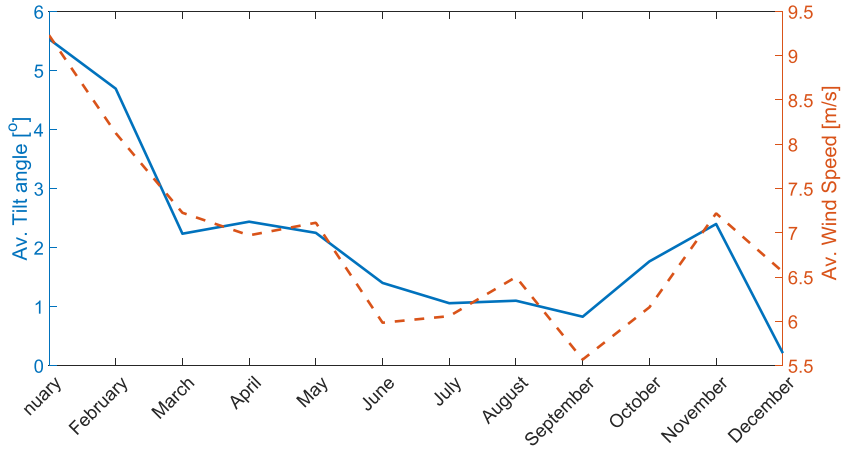


FIGURE 12 Average tilt angle for the floating photovoltaic (FPV) system and the average wind speed for year 2016 [Colour figure can be viewed at wileyonlinelibrary.com]

Figure 11 shows the wind speed, relative humidity, and also the relative difference between equilibrium temperatures $\Delta T_{Eq} = (T_{Eq,LBPV} - T_{Eq,FPV})/T_{Eq,FPV}$ for both systems. Although the relative humidity is not significantly different for both systems, the wind speed is more variable for FPV system compared with the LBPV. It is shown that excluding three last months of the year, the equilibrium temperature considering the wind and humidity effect is much lower for the FPV system, the average of temperature difference is 28.5% when a maximum of 82%.

For computing the energy yield from the FPV system, the GTI calculation is also required. As discussed in Section 2.1, the irradiation should be calculated regarding the tilt angle that is zeros for LBPV system and changing due to the waves for FPV system. Figure 12 shows both estimated average tilt angle and average wind speed in 2016, monthly. It is depicted how the wind speed changes the maximum tilt for every month. The average tilt angle has more variation during the winter season, when the irradiation is much lower than other times of the year.

Energy yield is possible to be computed regarding both performance conditions, that is, GTI and equilibrium temperature for both systems. Using the wave spectrum values for all days of year 2016, we can compare the GHI and the GTI of the FPV system for the whole year 2016 (we only had data for 9 days in December 2016), see Figure 13. The left axis in this figure shows both daily averaged GTI and GHI of the FPV system; the right axis shows the wind speed. It can be inferred from this figure that an increase in the wind speed can increase the GTI. This effect is more tangible in colder months of the year when the solar elevation angle is smaller.

Figure 14 shows the bar chart of the output energy for the year 2016 on the left axis, and on the right axis, the relative difference between output energy from two systems on land and at sea is shown, $([E_{FPV} - E_{LBPV}]/E_{LBPV})$. It illustrates that the FPV system in all months performs better compared with the land-based system. The

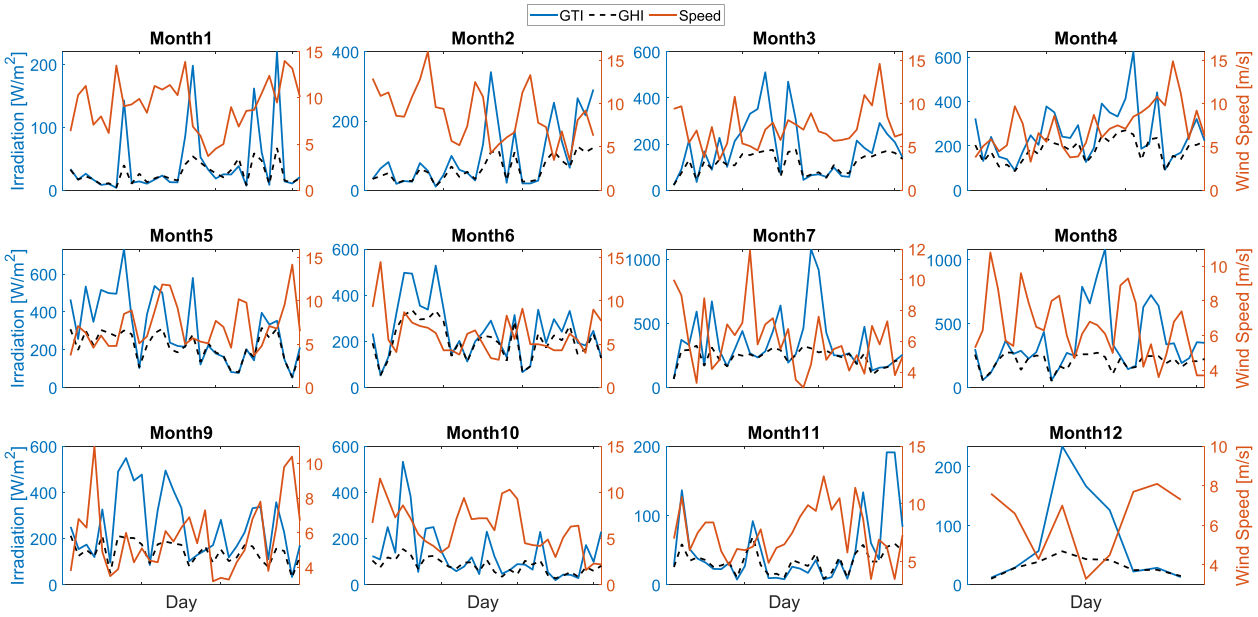


FIGURE 13 Daily averaged global horizontal irradiation (GHI) and irradiation on the tilted surface (GTI) in comparison to wind speed [Colour figure can be viewed at wileyonlinelibrary.com]

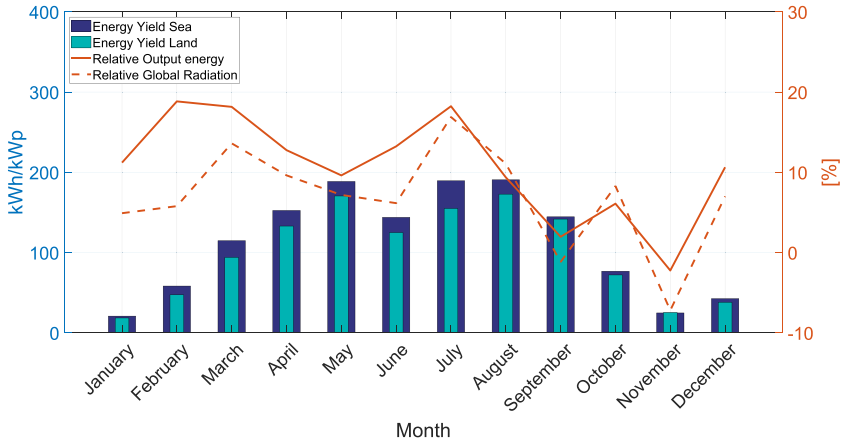


FIGURE 14 Left axis, normalized energy yield from two different systems. Right axis, relative output difference from two systems [Colour figure can be viewed at wileyonlinelibrary.com]

highest difference is seen for the month June, where the energy yield of the FPV system is 6% higher than the energy yield of the land system. In January, both systems perform quite similarly, and the relative difference is only almost 2%. On average, regarding this model and the 2016 data, the FPV system performs 3.49% better than the LBPV system. This result is lower than reported in literature, which was 10%[11] and 11%.[12] The annual yield for the LBPV system is 4.43×10^3 kWh (1,192 kWh/kWp) that is 12.96% less than FPV system that yields 5.01×10^3kWh (1346 kWh/kWp) in this year. However, it should be taken into consideration that the GHI is not similar in both locations and as depicted in Figure 14, GHI is about 8.54% higher in FPV location. Note further that the year 2016 was an exceptional year with a 5% higher annual irradiance than the 30-year average.[28]

To account for differences in irradiation, we calculate the performance ratio (PR), using the following equation:

$$PR = \frac{Y_f}{Y_r}, \tag{40}$$

where Y_f is final system yield from PV panel and Y_r is reference yield.

Figure 15 depicts PR for both systems, the average PR for the LBPV during the year 2016 is 81.66% and for FPV is 3.15% more and equal to 84.75%. For most months, PR values differ, and this reflects the temperature differences that occur in both systems.

Mathematical modeling and simulations implementing actual weather data for comparison between two similar PV systems on land and sea show that different ambient conditions affect the energy yield of the systems. Although the wind speed simultaneously changes the tilt angle, and as a result, the panels are not always positioned at the optimum angle, the existence of water around the pontoon is a big advantage for improving the efficiency, as the panel temperature is lower and more constant as well. We do note that the effect of dust on the LBPV system and salinity of water is neglected in this model for simplicity.

5 | CONCLUSION

A mathematical model for both land and sea PV systems has been developed in this work. To this end, both actual irradiation and temperature data are used for the modeling. A floating PV system is

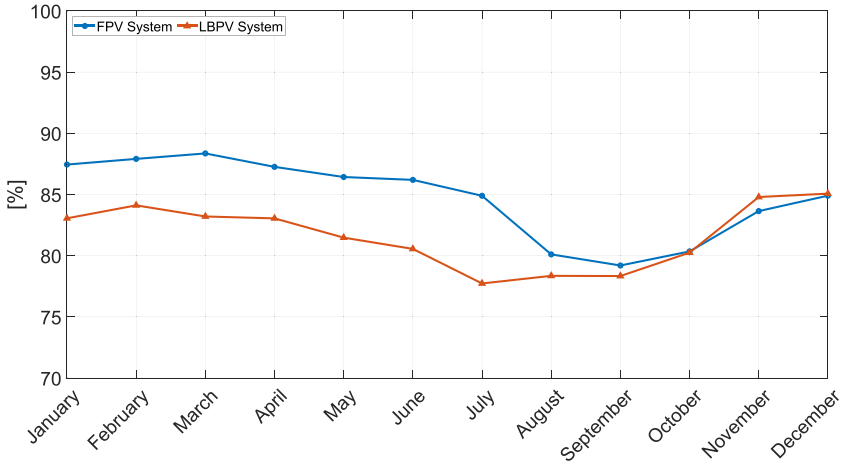


FIGURE 15 Performance ratio for both floating photovoltaic (FPV) and land-based photovoltaic (LBPV) systems [Colour figure can be viewed at wileyonlinelibrary.com]

characterized by constantly varying tilt angles, in contrast to a 4 system (assuming no tracking), which complicates energy yield modeling. A model has been developed that allows the calculation of the tilt angle variation based on wave characteristics and how these are influenced by wind speed leading to a wave spectrum analysis. Moreover, for calculating the temperature of the PV systems, both heat transfer theory and apparent temperature method are implemented to estimate an accurate equilibrium temperature, where the effect of wind speed, relative humidity, and presence of water is taken in to account.

Our simulations show that the energy yield of both systems differs predominantly as a result of lower temperatures. We found that the system at sea performs 12.96% better on average on an annual basis than the land-based system.

ACKNOWLEDGEMENT

The authors gratefully acknowledge fruitful discussions with Brigitte Vlaswinkel and Allard van Hoeken (Oceans of Energy) and Anne de Waal (UU). This work is partly financially supported by the Netherlands Enterprise Agency (RVO) within the framework of the Dutch Topsector Energy (project Comparative assesement of PV at Sea versus PV on Land, CSEALAND).

ORCID

S. Zahra Golroodbari https://orcid.org/0000-0002-5843-0463
Wilfried van Sark https://orcid.org/0000-0002-4738-1088

REFERENCES

1. Breyer C, Bogdanov D, Aghahosseini A, Gulagi A, Child M, Oyewo AS, Farfan J, Sadovskaia K, Vainikka P. Solar photovoltaics demand for the global energy transition in the power sector. *Prog Photovolt Res Appl*. 2018;26(8):505-523. https://onlinelibrary.wiley.com/doi/abs/10.1002/pip.2950
2. Jäger-Waldau A. Snapshot of photovoltaics–February 2019. *Energies*. 2019;12(769). http://www.mdpi.com/1996-1073/12/5/769
3. Cazzaniga R, Cicu M, Rosa-Clot M, Rosa-Clot P, Tina GM, Ventura C. Floating photovoltaic plants: performance analysis and design solutions. *Renew Sust Energ Rev*. 2018;81:1730-1741. http://www.sciencedirect.com/science/article/pii/S1364032117309103
4. Dupré O, Vaillon R, Green MA. *Thermal Behavior of Photovoltaic Devices – Physics and Engineering*: Springer International Publishing; 2017. https://hal.archives-ouvertes.fr/hal-01464274
5. Irgens Kuhnle T. All subsea—creating value from subsea processing. *DNVGL Strat Res Innov Pos Paper*. 2015;13(1):1-72. http://images.e.dnvgl.com/Web/DNVGL/%7B1c7ff232-8a89-4635-96dc-8c44fd3d3534%7D_DNVGL_All_subsea_position_paper.pdf
6. Wang Z, Carriveau R, Ting DavidS-K, Xiong W, Wang Z. A review of marine renewable energy storage. *International Journal of Energy Research*. 2019;0(0). in press, https://onlinelibrary.wiley.com/doi/abs/10.1002/er.4444
7. Pringle AM, Handler RM, Pearce JM. Aquavoltaics: synergies for dual use of water area for solar photovoltaic electricity generation and aquaculture. *Renew Sust Energ Rev*. 2017;80:572-584. http://www.sciencedirect.com/science/article/pii/S1364032117308304
8. Trapani K. Flexible floating thin film photovoltaic (PV) array concept for marine and lacustrine environments. *Ph.D. Thesis*; 2014.
9. Trapani K, Redón Santafé M. A review of floating photovoltaic installations: 2007–2013. *Prog Photovolt Res Appl*. 2015;23(4):524-532. https://onlinelibrary.wiley.com/doi/abs/10.1002/pip.2466
10. Rosa-Clot M, Tina GM. Chapter 5—the floating PV plant. In: Rosa-Clot Marco, Tina GiuseppeMarco, eds. *Submerged and Floating Photovoltaic Systems*: Academic Press; 2018:89-136. http://www.sciencedirect.com/science/article/pii/B9780128121498000053
11. Liu H, Krishna V, Lun Leung J, Reindl T, Zhao L. Field experience and performance analysis of floating PV technologies in the tropics. *Prog Photovolt Res Appl*. 2018;26(12):957-967. https://onlinelibrary.wiley.com/doi/abs/10.1002/pip.3039
12. Choi Y-K. A study on power generation analysis of floating PV system considering environmental impact. *Int J Softw Eng Appl*. 2014;8:75-84.
13. Cazzaniga R, Rosa-Clot M, Rosa-Clot P, Tina GM. Floating tracking cooling concentrating (FTCC) systems. In: 2012 38th IEEE Photovoltaic Specialists Conference; 2012June:000514-000519.
14. Rosa-Clot M, Tina GM. Chapter 4—submerged PV systems. In: Rosa-Clot Marco, Tina GiuseppeMarco, eds. *Submerged and Floating Photovoltaic Systems*: Academic Press; 2018:65-87. http://www.sciencedirect.com/science/article/pii/B9780128121498000041
15. Martín N, Ruiz JM. Annual angular reflection losses in PV modules. *Prog Photovolt Res Appl*. 2005;13(1):75-84. https://onlinelibrary.wiley.com/doi/abs/10.1002/pip.585
16. Klucher TM. Evaluation of models to predict insolation on tilted surfaces. *Solar Energy*. 1979;23(2):111-114.
17. Gulin M, Vašak M, Baotic M. Estimation of the global solar irradiance on tilted surfaces. In: 17th International Conference on Electrical Drives and Power Electronics (Edpe 2013), Vol. 6; 2013:347-353.
18. American National Snow and Ice Data (nsid). https://nsidc.org
19. Muetze A, Vining J. Ocean wave energy conversion—a survey. In: Industry Applications Conference, 2006. 41st IAS Annual Meeting. Conference Record of the 2006 IEEE, Vol. 3 IEEE; 2006:1410-1417.

20. Hasselmann K, Ross DB, Müller P, Sell W. A parametric wave prediction model. *J Phys Oceanogr*. 1976;6:200-228.
21. Yu Y, Pei H, Xu C. Parameter identification of JONSWAP spectrum acquired by airborne LIDAR. *J Ocean Univ China*. 2017;16(6):998-1002. https://doi.org/10.1007/s11802-017-3271-2
22. Asgeirsson GS. Hydrodynamic investigation of wavepower buoys. *Master's Thesis*: KTH, Naval Systems; 2013.
23. Servant J-M. Calculation of the cell temperature for photovoltaic modules from climatic data. In: Bilgen E., Hollands K. G. T., eds. *Intersol Eighty Five*. Oxford: Pergamon; 1986:1640-1643. http://www.sciencedirect.com/science/article/pii/B9780080331775503112
24. Huld T, Amillo A, Gracia M. Estimating PV module performance over large geographical regions: the role of irradiance, air temperature, wind speed and solar spectrum. *Energies*. Multidisciplinary Digital Publishing Institute. 2015;8(6):5159-5181. http://www.mdpi.com/1996-1073/8/6/5159
25. Jacobs SJ, Pezza AB, Barras V, Bye J, Vihma T. An analysis of the meteorological variables leading to apparent temperature in australia: present climate, trends, and global warming simulations. *Global Planetary Change*. 2013;107:145-156. http://www.sciencedirect.com/science/article/pii/S0921818113001343
26. Steadman RG. Norms of apparent temperature in Australia. *Aust Meteorol Mag*. 1994;43(1):1-16. https://www.scopus.com/inward/record.uri?eid=2-s2.0-0028599599&partnerI%D=40&md5=ed69a1333f1e840586a01558670772cc
27. Lawrence MG. The relationship between relative humidity and the dewpoint temperature in moist air: a simple conversion and applications. *Bull Amer Meteor Soc*. 2005;86(2):225-234. https://doi.org/10.1175/BAMS-86-2-225
28. Institute TRNM. Dutch National Weather Service. https://www.knmi.nl
29. Van Sark W, Louwen A, de Waal AC, Schropp R. Upot: the Utrecht photovoltaic outdoor test facility. In: 27th European Photovoltaic Solar Energy Conference and Exhibition WIP Munich, Germany; 2012:3247-3249.
30. Pinet PR. *Invitation to Oceanography - 7th Edition* -: Jones And Bartlett Publishers, Inc; 2014.
31. Laboratories SN. PV_LIB toolbox. https://pvpmc.sandia.gov/applications/pv_lib-toolbox/
32. Burges CJC. A tutorial on support vector machines for pattern recognition. *Data Min Knowl Disc*. 1998;2:1-43. http://www.cmap.polytechnique.fr/mallat/papiers/svmtutorial.pdf
33. Suykens Johan AK, Van Gestel T, De Brabanter J, et al. *Least Squares Support vector Machines*, Vol. 4: World Scientific; 2002.
34. Energy V. SmartSolar MPPT 75/15, www.victronenergy.com. https://www.victronenergy.com/contact
35. Hou Y, Li H, Zhao L, Wang Y. Temperature-related power loss modeling for buck converter. *IEICE Elect Express*. 2017;14(6):20170004-20170004.

How to cite this article: Golroodbari SZ, van Sark W. Simulation of performance differences between offshore and land-based photovoltaic systems. *Prog Photovolt Res Appl*. 2020;28:873–886. https://doi.org/10.1002/pip.3276